J. Fluid Mech. (1995), *vol.* 305, *pp.* 1–27

Unsteady separation and heat transfer upstream of obstacles

By **R. I. PUHAK, A. T. DEGANI** AND **J. D. A. WALKER**
Department of Mechanical Engineering and Mechanics, Lehigh University,
Bethlehem, PA 18015, USA

(Received 10 March 1995 and in revised form 10 July 1995)

The development of a laminar boundary layer upstream of both two- and three-dimensional obstacles mounted on a plane wall is considered. The motion is impulsively started from rest, and it is shown that the boundary layer upstream of the obstacle initially develops independently from that on the obstacle itself. Numerical solutions for the unsteady boundary-layer flow on the plane wall are obtained in both Eulerian and Lagrangian coordinates. It is demonstrated that in both situations the flow focuses into a narrow-band eruption characteristic of separation phenomena at high Reynolds number. For the three-dimensional problem, results are obtained on a symmetry plane upstream of the obstacle which indicate the evolution, and subsequent sharp compression, of a spiral vortex in the near-wall flow in a manner consistent with recent experimental studies. The eruptive response of the two-dimensional boundary layer is found to be considerably stronger than the corresponding event in three dimensions. Calculated results for the temperature distribution are obtained for the situation where the wall temperature is constant but different from that of the mainstream. It is shown that a concentrated response develops in the surface heat transfer rate as the boundary layer starts to separate from the surface.

1. Introduction

Situations where a developing boundary layer on a wall encounters an obstacle downstream are commonplace. In this study, obstacles having a height much larger than the boundary-layer thickness are considered and, in such circumstances, a strong adverse pressure gradient is induced upstream of the obstruction. Two specific (but representative) obstacles are studied in detail, namely (i) a three-dimensional obstacle consisting of a circular cylinder mounted normal to a flat plate, and (ii) a two-dimensional ridge constituting half a circular cylinder mounted on a plane wall. A schematic diagram of both obstacles is shown in figure 1 along with the boundary-layer structure expected for a high Reynolds number laminar flow. In both configurations, a polar coordinate system is defined with origin at the cylinder centre. In this study the principal interest is in the boundary layer upstream of the obstacles which is labelled region 1 in figure 1 and which is defined by $\theta \rightarrow \pi$. Let U denote the speed of the inviscid motion at large distances upstream, with the flow being from left to right; in both situations the mainstream flow just outside the boundary layer is decelerated to rest at a stagnation point in front of the obstacle. For the two-dimensional ridge, fluid particles just outside the boundary layer are then accelerated away from near the frontal stagnation point up and over the obstacle; on the other hand, in the three-dimensional flow, fluid particles near the symmetry plane are eventually deflected around the cylinder upon approach to the frontal stagnation region. In both situations,

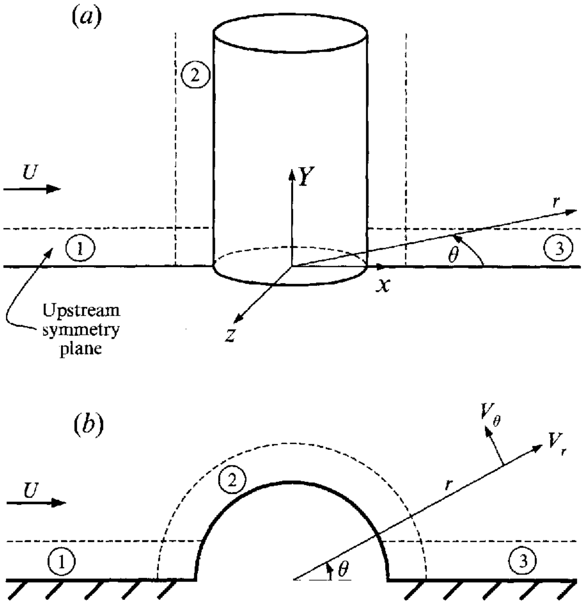

FIGURE 1. Sketch of the geometry and boundary-layer structure (not to scale): (*a*) circular cylinder mounted normal to a wall, (*b*) two-dimensional ridge.

the upstream boundary layer is exposed to a streamwise pressure gradient which is purely adverse; for high Reynolds numbers *Re*, recent theoretical developments (Van Dommelen & Shen 1982; Elliott, Cowley & Smith 1983; Cowley, Van Dommelen & Lam 1990) suggest that under such circumstances the upstream boundary layer will separate in an inherently unsteady process leading to a local boundary-layer eruption. Here, following Sears & Telionis (1975) and Van Dommelen & Shen (1980), the term separation is used to denote a process wherein a thin boundary layer develops strong outflows and starts to interact with the external flow for the first time, thereby separating from the surface.

Consequently, it appears that the upstream boundary-layer motion may be inherently unsteady at high *Re* and exhibit a tendency to interact strongly with the external flow intermittently. Recent experimental and computational studies support this expectation. Acarlar & Smith (1987) observed the fluid motion within a subcritical boundary layer in the vicinity of a hemispherical bump mounted on a flat plate, as well as that associated with a variety of other similar obstacles. In all situations, the flow near the obstacle was found to be inherently unsteady and characterized by the periodic creation of hairpin vortices in a sequence of events apparently related to a viscous–inviscid interaction with boundary layers in the vicinity of the obstacle. A similar but somewhat more complex phenomenon has been observed by Smith, Fitzgerald & Greco (1991) in their study of the motion past the cylindrical obstacle shown in figure 1(*a*). In this geometry, necklace vortices were observed to form and wrap around the obstacle, having legs that trail downstream of the cylinder. At sufficiently high *Re*, the vortex motion near the cylinder is inherently unsteady with new necklace vortices apparently forming near the upstream symmetry plane and subsequently spreading outward to engirdle the obstacle. At a certain stage, a sharply eruptive process in the vicinity of the upstream symmetry plane appears to lead to the release of each necklace vortex (Doligalski, Smith & Walker 1994) which is then convected downstream toward the cylinder. The endwall boundary layer is observed to be laminar over a wide range of large Reynolds numbers, but as a consequence of the vortex-creation processes in the vicinity of the obstacle, the motion there is an unsteady complex periodic flow. Recently Visbal (1991) and Hung, Sung & Chen (1991) have calculated this flow development at moderate Reynolds numbers using a simulation based on the full three-dimensional Navier–Stokes equations. In both studies, a periodic behaviour was found corresponding to vortex evolution and subsequent vortex release in a manner qualitatively similar to that observed by Smith *et al.* (1991). Unfortunately, the full three-dimensional problem is extremely complex and because of computer limitations, Visbal (1991) found it was not possible to adequately resolve a number of features of the unsteady flow or to extend the calculations into the high Reynolds number regime.

In the present study, the boundary-layer development in the limit of large Reynolds number will be considered for both obstacles shown in figure 1. The flow is taken to be impulsively started from rest since this is the simplest possible initial condition. Here the main objective is to understand the nature of the flow field at later times and whether or not strong interactions occur; therefore, the initial condition used may be regarded as mathematically convenient and the simplest way of ascertaining why periodic eruptions are observed in the experiments. Immediately after the impulsive start, a set of thin boundary layers forms on all solid surfaces (as shown in figure 1), and outside these layers the motion is initially inviscid and irrotational. If all velocities and lengths are made dimensionless with respect to the flow speed at infinity U and the cylinder radius a, the inviscid flow has radial and polar velocities given by

$$V_r = \left(1-\frac{1}{r^2}\right)\cos\theta, \quad V_\theta = -\left(1+\frac{1}{r^2}\right)\sin\theta, \tag{1}$$

respectively, in both cases. The inviscid flow remains unaltered until one or more of the boundary layers becomes eruptive, thereby introducing vorticity into the external flow. In the following sections the nature of the boundary-layer development will be examined for both the two- and three-dimensional problems with the main emphasis on the upstream layer. Critical features for the three-dimensional problem occur on the upstream symmetry plane and attention will be focused there in this study. Although only two specific obstacles will be examined in detail here, it will be argued that the flow development should be similar for a range of similar obstructions.

In many applications, such as gas turbines, heat transfer occurs in the endwall boundary layer, and it is of interest to understand the influence of the unsteady flow structure on the surface heat flux. For both obstacles, calculations were carried out for the evolving temperature field in the boundary layer for the case where the wall is maintained at a constant but different temperature from that of the mainstream. The results indicate that the developing unsteady flow in the boundary layer has a significant influence on the surface heat transfer rate, which develops sharp streamwise variations as the boundary layer proceeds toward separation.

2. The Eulerian formulation

Consider first the formulation for the symmetry plane in the three-dimensional problem; it will be subsequently shown that the two-dimensional ridge can be viewed as a subset of this formulation. As depicted schematically in figure 1(*a*), upstream and downstream symmetry surfaces occur in the plane $z = 0$, and here the boundary layers (labelled 1 and 3 in figure 1*a*) develop independently of the other shear layers that occur on the endwall and the cylinder, at least for an initial period following the impulsive start (Ersoy & Walker 1987). A Cartesian coordinate system (x, Y, z), with origin at the centre of the base of the cylinder, is adopted with corresponding velocity components (u, V, w); here all lengths and velocities are made dimensionless with respect to the cylinder radius a and the uniform flow speed U far from the obstruction, respectively. The Reynolds number, defined by $Re = Ua/\nu$, is assumed large where ν is the kinematic viscosity. Scaled boundary-layer variables are defined by

$$y = Re^{1/2}\,Y, \quad v = Re^{1/2}\,V, \tag{2}$$

and in the vicinity of the symmetry planes, the velocity components have the form (Ersoy & Walker 1987)

$$u = u(x,y,t)+O(z^2), \quad v = v(x,y,t)+O(z^2), \quad w = z\tilde{w}(x,y,t)+O(z^3), \tag{3}$$

where $\tilde{w} = \lim_{z\to 0}\partial w/\partial z$. Upon defining a dimensionless temperature difference by

$$\theta = \frac{T-T_s}{T_\infty - T_s}, \tag{4}$$

it follows that since the temperature field is also symmetric about the plane $z = 0$,

$$\theta = \theta(x,y,t)+O(z^2), \tag{5}$$

for small z. Thus the boundary-layer equations describing the flow on the symmetry plane are

$$\frac{\partial u}{\partial x}+\frac{\partial v}{\partial y}+\tilde{w} = 0, \tag{6}$$

$$\frac{\partial u}{\partial t}+u\frac{\partial u}{\partial x}+v\frac{\partial u}{\partial y} = U_\infty\frac{\mathrm{d}U_\infty}{\mathrm{d}x}+\frac{\partial^2 u}{\partial y^2}, \tag{7}$$

$$\frac{\partial \tilde{w}}{\partial t}+u\frac{\partial \tilde{w}}{\partial x}+v\frac{\partial \tilde{w}}{\partial y}+\tilde{w}^2 = U_\infty\frac{\mathrm{d}\tilde{W}_\infty}{\mathrm{d}x}+\tilde{W}_\infty^2+\frac{\partial^2 \tilde{w}}{\partial y^2}, \tag{8}$$

$$\frac{\partial \theta}{\partial t}+u\frac{\partial \theta}{\partial x}+v\frac{\partial \theta}{\partial y} = \frac{1}{Pr}\frac{\partial^2 \theta}{\partial y^2}, \tag{9}$$

where Pr is the Prandtl number and $U_\infty(x)$, $\tilde{W}_\infty(x)$ are the mainstream velocity distributions at the boundary-layer edge. It may be shown using equations (1) that

$$U_\infty(x) = 1-\frac{1}{x^2}, \quad \tilde{W}_\infty(x) = -\frac{2}{x^3}. \tag{10a,b}$$

On the upstream symmetry plane (labelled 1 in figure 1a) where x lies in the range $(-\infty, -1)$, the external streamwise velocity decelerates from 1 to rest at the cylinder, and near the plane the spanwise flow is away from the plane $z = 0$; here the boundary layer is exposed to a purely adverse streamwise pressure gradient. On the downstream symmetry plane (labelled 3 in figure 1a), the external streamwise velocity accelerates away from the cylinder at $x = 1$ to a unit speed as $x\to\infty$, the spanwise flow is toward the symmetry plane, and the boundary layer is exposed to a continuously favourable streamwise pressure gradient. Evidently, the most interesting behaviour can be expected on the upstream symmetry plane.

The continuity equation (6) can be identically satisfied by introducing two functions ϕ and ψ defined by

$$u = \frac{\partial \psi}{\partial y}, \quad v = -\frac{\partial \psi}{\partial x}-\phi, \quad \tilde{w} = \frac{\partial \phi}{\partial y}. \tag{11a–c}$$

In view of the impulsive-start condition, Rayleigh variables are introduced according to

$$n = \frac{y}{2t^{1/2}}, \quad \psi = 2t^{1/2}\,U_\infty(x)\,\Psi(x,n,t), \quad \phi = 2t^{1/2}\,\tilde{W}_\infty(x)\,\Phi(x,n,t), \qquad (12\,a\text{–}c)$$

and it is convenient to write the governing equations in terms of normalized velocity components u_1 and u_2 defined by

$$u = U_\infty u_1, \quad \tilde{w} = \tilde{W}_\infty u_2. \qquad (13)$$

It is easily shown that $u_1 = \partial\Psi/\partial n$ and $u_2 = \partial\Phi/\partial n$. In addition, to allow a compact notation, the dimensionless temperature difference will be denoted by $u_3 = \theta$; then the independent variables (u_1, u_2, u_3) all vary from 0 to 1 across the boundary layer and satisfy equations derived from (7)–(9) which are of the form

$$4t\frac{\partial u_i}{\partial t} = T_i\frac{\partial^2 u_i}{\partial n^2} + P\frac{\partial u_i}{\partial n} + Q\frac{\partial u_i}{\partial x} + 4tW_i u_i + 4t\Gamma_i, \qquad (14)$$

$i = 1, 2, 3$. (Note that no summation is implied in (14).) The coefficients in (14) are given by

$$P = 2n + 4t\left\{U'_\infty\,\Psi + U_\infty\frac{\partial\Psi}{\partial x} + \tilde{W}_\infty\,\Phi\right\}, \quad Q = -4tU_\infty u_1, \qquad (15)$$

and

$$T_1 = 1, \quad \Gamma_1 = U'_\infty(x), \quad W_1 = -U'_\infty(x)\,u_1, \qquad (16)$$

$$T_2 = 1, \quad \Gamma_2 = \frac{U_\infty \tilde{W}'_\infty}{\tilde{W}_\infty} + \tilde{W}_\infty, \quad W_2 = -\frac{U_\infty \tilde{W}'_\infty}{\tilde{W}_\infty}u_1 - \tilde{W}_\infty u_2, \qquad (17)$$

$$T_3 = 1/Pr, \quad \Gamma_3 = W_3 = 0. \qquad (18)$$

Here the prime denotes differentiation with respect to x.

The boundary conditions associated with the system (14) are

$$u_i = 0 \quad \text{at} \quad n = 0; \quad u_i \to 1 \quad \text{as} \quad n \to \infty. \qquad (19)$$

As $t \to 0$, equations (14) reduce to

$$T_i\frac{\partial^2 u_i}{\partial n^2} + 2n\frac{\partial u_i}{\partial n} = 0, \qquad (20)$$

for $i = 1, 2, 3$ and the solutions, satisfying conditions (19) are

$$u_1 = u_2 = \operatorname{erf} n, \quad u_3 = \operatorname{erf}(n\,Pr^{1/2}), \qquad (21)$$

which define the initial conditions for the system (14). As $x \to \pm\infty$, $U_\infty \to 1$ and $\tilde{W}_\infty \to 0$ and the system (14) also reduces to (20); thus (21) also provides the boundary conditions as $x \to \pm\infty$ for all t. Finally, both upstream and downstream boundary layers develop independently of one another initially, and the solutions at the stagnation points give the final set of boundary conditions. It may be shown that (14) becomes

$$4t\frac{\partial u_i}{\partial t} = T_i\frac{\partial^2 u_i}{\partial n^2} + \left\{2n + 4t(U'_\infty\,\Psi + \tilde{W}_\infty\,\Phi)\right\}\frac{\partial u_i}{\partial n} + 4t\chi_i, \qquad (22)$$

at the stagnation points $x = \pm 1$, respectively, where

$$\chi_1 = U'_\infty (1-u_1^2), \quad \chi_2 = \tilde{W}_\infty (1-u_2^2), \quad \chi_3 = 0. \tag{23}$$

Note that in (22) and (23), U'_∞ and $\tilde{W}_\infty$ are evaluated at $x = \pm 1$ using (10). The stagnation-point solutions also satisfy the boundary conditions (19) with initial conditions (21) and must be found numerically. The formulation in (14)–(23) applies to a general flow in a plane of symmetry. The two-dimensional equations may be easily obtained by discarding the cross-stream momentum equation ($i = 2$) and substituting $\tilde{W}_\infty \equiv 0$ in the streamwise momentum ($i = 1$) and energy ($i = 3$) equations. For the specific case considered here, the external velocity distribution for the plane-of-symmetry problem is given by (10). For the two-dimensional problem, the streamwise velocity distribution is the same and $\tilde{W}_\infty \equiv 0$.

Starting from the initial conditions (21), the objective is to advance the solution of (14) and (22) forward in time. It is convenient to introduce transformations of the form

$$x = h_x(\hat{x}), \quad n = k_n \tan(\tfrac{1}{2}\pi\hat{n}). \tag{24a,b}$$

Here the variables $(\hat{x}, \hat{n})$ will be referred to as computational coordinates and are introduced in order that: (i) the calculations are performed on a domain of finite extent, and (ii) grid points may be clustered in regions in the physical domain where intense variations develop in the flow properties. Two transformations were considered for the streamwise direction, corresponding to different mappings $h_x(\hat{x})$, and each will be described subsequently; in both cases, the physical streamwise extent was mapped onto the interval $(0, 1]$. The second of transformations (24) maps the range $[0, \infty)$ in n to $[0, 1)$ in $\hat{n}$; here k_n is a parameter which controls the mesh spacing in the physical space, with smaller values of k_n producing a more concentrated mesh near the wall (for a uniform mesh in $\hat{n}$). In computational coordinates, the system (14) becomes

$$4t\frac{\partial u_i}{\partial t} = \hat{T}_i \frac{\partial^2 u_i}{\partial \hat{n}^2} + \hat{P}\frac{\partial u_i}{\partial \hat{n}} + \hat{Q}\frac{\partial u_i}{\partial \hat{x}} + 4tW_i u_i + 4t\Gamma_i, \tag{25}$$

where

$$\hat{T}_i = Z^2(\hat{n}) T_i, \quad Z(\hat{n}) = \frac{2}{\pi k_n}\cos^2(\tfrac{1}{2}\pi\hat{n}), \quad \hat{Q} = Q/h'_x(\hat{x}), \tag{26}$$

and

$$\hat{P} = Z'(\hat{n})\left(Z(\hat{n})\,T_i - \frac{2k_n}{\pi}\right) + 4tZ(\hat{n})\left\{U'_\infty(x)\,\Psi + \frac{U_\infty}{h'_x(\hat{x})}\frac{\partial \Psi}{\partial \hat{x}} + \tilde{W}_\infty \Phi\right\}. \tag{27}$$

The primes denote differentiation with respect to the argument.

Two streamwise transformations were used in the course of the integrations. The downstream symmetry plane involves a boundary-layer motion in a purely favourable pressure gradient; consequently, it emerges that the flow development does not contain any interesting features and results will be presented only for the upstream boundary layer, where the pressure gradient is everywhere adverse. The first mapping will be referred to as the 'algebraic' transformation and has

$$x = h_x(\hat{x}) = -1/\hat{x}, \quad h'_x(\hat{x}) = 1/\hat{x}^2. \tag{28}$$

In view of (10*a*), this is akin to a Görtler transformation. For a uniform mesh spacing in $\hat{x}$, this mapping clusters points in the physical space near the stagnation point defined by $\hat{x} = 1$. The second transformation will be referred to as the 'tangent' transformation; it was developed pragmatically based on the observation that an intense streamwise variation in the flow field was eventually found to occur (using the algebraic transformation) at a location, denoted by x_o, upstream of the stagnation point. Consider the mapping

$$x = h_x(\hat{x}) = x_o + k_x \tan\left[\frac{\pi}{2}\left(\frac{\hat{x}}{\hat{x}_o} - 1\right)\right], \tag{29}$$

where k_x is a constant and

$$\frac{1}{\hat{x}_o} = 1 + \frac{2}{\pi}\arctan\left[-\frac{(1+x_o)}{k_x}\right]. \tag{30}$$

It may easily be confirmed that this mapping is one-to-one for $-\infty < x \leqslant -1$ and specifically that $x = -\infty$, x_o, -1 transform to $\hat{x} = 0$, $\hat{x}_o$, 1, respectively. Upon differentiating (29), it follows that

$$h_x'(\hat{x}) = \frac{\pi k_x}{2\hat{x}_o}\sec^2\left[\frac{\pi}{2}\left(\frac{\hat{x}}{x_o} - 1\right)\right], \tag{31}$$

which is a minimum at $\hat{x} = \hat{x}_o$, for fixed k_x and $\hat{x}_o$; consequently, the maximum clustering of points occurs in physical space at $x = x_o$. The parameter k_x controls the resolution near x_o, with a smaller value of k_x producing a finer mesh in physical space near x_o. The specific choice of x_o and k_x was motivated from a preliminary set of results obtained using the algebraic transformation (28) and will be discussed subsequently.

The numerical integrations may be carried out efficiently and with good accuracy in the Eulerian formulation for a substantial portion of the total integration time. However, the boundary layer on the upstream symmetry plane eventually develops strong outflows and evolves toward a sharply focused eruption. As discussed by Van Dommelen & Shen (1980, 1982), Cowley *et al.* (1990) and Peridier, Smith & Walker (1991), it is generally not possible to make progress with an Eulerian integration under such circumstances unless some type of time-dependent adaptive remeshing algorithm is adopted (see, for example, Adams, Conlisk & Smith 1995). However, it is believed that the most attractive alternative is to continue the calculations in Lagrangian coordinates, which are described next.

3. Lagrangian formulation

The advantages of the Lagrangian description for the calculation of eruptive boundary layers were originally described by Van Dommelen & Shen (1980, 1982) for two-dimensional flows and the approach in three dimensions has recently been discussed by Van Dommelen & Cowley (1990) and Cowley *et al.* (1990). Let (ξ, η, ζ, t') denote Lagrangian coordinates with (ξ, η) and ζ denoting the initial particle positions in the symmetry plane and the initial normal distance of a particle from the symmetry plane, respectively; t' denotes time in the Lagrangian system. Fluid particles initially on the symmetry plane remain there for all time (except perhaps at isolated points), and since $z(\xi, \eta, \zeta, t')$ is expected to be a regular function, it follows from a Taylor series expansion that the z particle positions near the symmetry plane at $\zeta = 0$ have the form

$$z(\xi, \eta, \zeta, t') = \zeta\tilde{z}(\xi, \eta, t') + \ldots, \tag{32}$$

where $\tilde{z} = \lim_{\zeta\to 0} \partial z/\partial\zeta$. It follows that on the symmetry plane

$$\frac{\partial z}{\partial \xi} = \frac{\partial z}{\partial \eta} = 0 \quad \text{at} \quad \zeta = 0. \tag{33}$$

In addition, the spanwise velocity vanishes on the symmetry plane (cf. (3)) and near the symmetry plane is of the form

$$w = z\tilde{w} = \zeta\tilde{z}(\xi,\eta,t')\,\tilde{w}(\xi,\eta,t')+\dots. \tag{34}$$

Since $w = \partial z/\partial t'$, it follows that $\tilde{z}$ and $\tilde{w}$ are related by

$$\frac{\partial \tilde{z}}{\partial t'} = \tilde{z}\tilde{w}. \tag{35}$$

The transformation laws from the Eulerian system (x, y, z, t) to the Lagrangian are given in the Appendix. The continuity equation (6) becomes

$$\tilde{z}\left\{\frac{\partial x}{\partial \xi}\frac{\partial y}{\partial \eta}-\frac{\partial x}{\partial \eta}\frac{\partial y}{\partial \xi}\right\}=1, \tag{36}$$

and the momentum and energy equations (7)–(9) transform to

$$\frac{\partial u}{\partial t'} = U_\infty\frac{\mathrm{d}U_\infty}{\mathrm{d}x}+\mathrm{D}_y^2 u,\quad \frac{\partial \tilde{w}}{\partial t'} = U_\infty\frac{\mathrm{d}\tilde{W}_\infty}{\mathrm{d}x}+\tilde{W}_\infty^2-\tilde{w}^2+\mathrm{D}_y^2\tilde{w},\quad \frac{\partial \theta}{\partial t'}=\frac{1}{Pr}\mathrm{D}_y^2\theta, \tag{37a–c}$$

where the operator D_y is defined by

$$\mathrm{D}_y = \tilde{z}\left\{\frac{\partial x}{\partial \xi}\frac{\partial}{\partial \eta}-\frac{\partial x}{\partial \eta}\frac{\partial}{\partial \xi}\right\}. \tag{38}$$

The associated equations for x and $\tilde{z}$ are

$$\frac{\partial x}{\partial t'} = u,\quad \frac{\partial}{\partial t'}(\log|\tilde{z}|) = \tilde{w}, \tag{39}$$

and the boundary conditions are

$$u=\tilde{w}=\theta=0 \quad\text{at}\quad \eta=0,\qquad u\to U_\infty,\quad \tilde{w}\to\tilde{W}_\infty,\quad \theta\to 1\quad\text{as}\quad \eta\to\infty. \tag{40}$$

The initial conditions follow from (A 7) and are

$$x=\xi,\quad y=\eta,\quad \tilde{z}=1\quad\text{at}\quad t'=t_0 \tag{41}$$

for all (ξ,η), along with specified distributions of $u(\xi,\eta,t')$, $\tilde{w}(\xi,\eta,t')$ at the initial instant t_0.

As in the Eulerian formulation, it is convenient to introduce normalized variables defined by (13), where now u_1 and u_2 are functions of (ξ,η,t'). It is readily shown that (37a) and (37b) become

$$\frac{\partial u_1}{\partial t'} = \frac{\mathrm{d}U_\infty}{\mathrm{d}x}(1-u_1^2)+\mathrm{D}_y^2 u_1, \tag{42a}$$

$$\frac{\partial u_2}{\partial t'} = \frac{U_\infty}{\tilde{W}_\infty}\frac{\mathrm{d}\tilde{W}_\infty}{\mathrm{d}x}(1-u_1u_2)+\tilde{W}_\infty(1-u_2^2)+\mathrm{D}_y^2 u_2. \tag{42b}$$

Again computational coordinates are defined on finite intervals according to transformations of the form

$$x=h_x(\hat{x}),\quad \xi=h_\xi(\hat{\xi}),\quad \eta=k_\eta\tan(\tfrac{1}{2}\pi\hat{\eta}), \tag{43a–c}$$

defining $\hat{x}$, $\hat{\xi}$, and $\hat{\eta}$ in the interval (0, 1); here k_η is a parameter which can be selected to control the spacing of the mesh normal to the wall and h_x and h_ξ are mapping functions which will subsequently be described. If the temperature variable θ is denoted by u_3, equations (37*c*), (42*a*) and (42*b*) are all of the form

$$A_i\frac{\partial u_i}{\partial t'} = \bar{R}\frac{\partial^2 u_i}{\partial \hat{\xi}^2}+\bar{S}\frac{\partial^2 u_i}{\partial \hat{\xi}\,\partial \hat{\eta}}+\bar{T}\frac{\partial^2 u_i}{\partial \hat{\eta}^2}+\bar{P}\frac{\partial u_i}{\partial \hat{\eta}}+\bar{Q}\frac{\partial u_i}{\partial \hat{\xi}}+\bar{W}_i u_i+\bar{\Gamma}_i, \tag{44}$$

for $i = 1, 2, 3$, where the coefficients are defined by

$$\bar{R} = \Pi\left(\frac{\partial \hat{x}}{\partial \hat{\eta}}\right)^2, \quad \bar{S} = -2\Pi\left(\frac{\partial \hat{x}}{\partial \hat{\xi}}\right)\left(\frac{\partial \hat{x}}{\partial \hat{\eta}}\right), \quad \bar{T} = \Pi\left(\frac{\partial \hat{x}}{\partial \hat{\xi}}\right)^2, \tag{45a–c}$$

$$\bar{P} = \Pi\left\{\frac{\partial \hat{x}}{\partial \hat{\xi}}\frac{\partial^2 \hat{x}}{\partial \hat{\xi}\,\partial \hat{\eta}}-\frac{\partial \hat{x}}{\partial \hat{\eta}}\frac{\partial^2 \hat{x}}{\partial \hat{\xi}^2}+\frac{h''_\xi(\hat{\xi})}{h'_\xi(\hat{\xi})}\frac{\partial \hat{x}}{\partial \hat{\xi}}\frac{\partial \hat{x}}{\partial \hat{\eta}}+\frac{Z'(\hat{\eta})}{Z(\hat{\eta})}\left(\frac{\partial \hat{x}}{\partial \hat{\xi}}\right)^2+\frac{1}{\tilde{z}}\frac{\partial \hat{x}}{\partial \hat{\xi}}\left\{\frac{\partial \hat{x}}{\partial \hat{\xi}}\frac{\partial \tilde{z}}{\partial \hat{\eta}}-\frac{\partial \hat{x}}{\partial \hat{\eta}}\frac{\partial \tilde{z}}{\partial \hat{\xi}}\right\}\right\}, \tag{45d}$$

$$\bar{Q} = \Pi\left\{\frac{\partial \hat{x}}{\partial \hat{\eta}}\frac{\partial^2 \hat{x}}{\partial \hat{\xi}\,\partial \hat{\eta}}-\frac{\partial \hat{x}}{\partial \hat{\xi}}\frac{\partial^2 \hat{x}}{\partial \hat{\eta}^2}+\frac{h''_\xi(\hat{\xi})}{h'_\xi(\hat{\xi})}\left(\frac{\partial \hat{x}}{\partial \hat{\eta}}\right)^2-\frac{Z'(\hat{\eta})}{Z(\hat{\eta})}\frac{\partial \hat{x}}{\partial \hat{\xi}}\frac{\partial \hat{x}}{\partial \hat{\eta}}+\frac{1}{\tilde{z}}\frac{\partial \hat{x}}{\partial \hat{\eta}}\left\{\frac{\partial \hat{x}}{\partial \hat{\eta}}\frac{\partial \tilde{z}}{\partial \hat{\xi}}-\frac{\partial \hat{x}}{\partial \hat{\xi}}\frac{\partial \tilde{z}}{\partial \hat{\eta}}\right\}\right\}, \tag{45e}$$

where the primes denote differentiation with respect to the argument, and

$$Z(\hat{\eta}) = \frac{2}{\pi k_\eta}\cos^2(\tfrac{1}{2}\pi\hat{\eta}), \quad \Pi = \left\{\frac{h'_x(\hat{x})}{h'_\xi(\hat{\xi})}Z(\hat{\eta})\,\tilde{z}\right\}^2; \tag{45f,g}$$

in addition,

$$A_1 = A_2 = 1, \quad A_3 = Pr, \tag{45h–j}$$

$$\bar{W}_1 = \frac{\mathrm{d}U_\infty}{\mathrm{d}x}u_1, \quad \bar{\Gamma}_1 = \frac{\mathrm{d}U_\infty}{\mathrm{d}x}, \tag{45k,l}$$

$$\bar{W}_2 = -\frac{U_\infty}{\tilde{W}_\infty}\frac{\mathrm{d}\tilde{W}_\infty}{\mathrm{d}x}u_1-\tilde{W}_\infty u_2, \quad \bar{\Gamma}_2 = \frac{U_\infty}{\tilde{W}_\infty}\frac{\mathrm{d}\tilde{W}_\infty}{\mathrm{d}x}+\tilde{W}_\infty, \tag{45m,n}$$

and $\bar{W}_3 = \bar{\Gamma}_3 = 0$. Finally, the associated equations for $\hat{x}$ and $\tilde{z}$ are

$$\frac{\partial \hat{x}}{\partial t'} = \frac{u_1 U_\infty}{h'_x}, \quad \frac{\partial}{\partial t'}(\log|\tilde{z}|) = u_2\tilde{W}_\infty. \tag{46}$$

Henceforth, the prime on the time variable t' will be dropped for convenience.

Next the boundary conditions are considered. From the definitions of the normalized velocities and temperature, it follows that

$$u_i = 0 \quad \text{at} \quad \hat{\eta} = 0; \qquad u_i \to 1 \quad \text{as} \quad \hat{\eta}\to 1. \tag{47}$$

The transformations introduced in (43) will be selected so that $\hat{\xi} = 0$ corresponds to locations far upstream of the obstacle (defined by $\xi \to -\infty$), and here (as previously discussed) the solution is a plane-parallel Rayleigh flow (cf. (21)). Consequently,

$$y = \eta, \quad u_1 = u_2 = \operatorname{erf}\left(\frac{\eta}{2t^{1/2}}\right) \quad u_3 = \operatorname{erf}\left(\frac{\eta}{2(Prt)^{1/2}}\right), \tag{48}$$

at $\hat{\xi} = 0$ for all t. The final boundary condition applies at the stagnation point immediately upstream of the obstacle defined by $\xi \to -1$ or, in transformed coordinates, by $\hat{\xi}\to 1$. Fluid particles which are initially at the stagnation point remain at that same value of x for all t, and hence $\partial x/\partial\eta = 0$ at $\xi = -1$. Furthermore, x may be written as a Taylor series about $\xi = -1$ according to

$$x(\xi, \eta, t) = -1 + (\xi + 1)\tilde{x}(\eta, t) + \ldots, \quad \tilde{x} = \left.\frac{\partial x}{\partial \xi}\right|_{\xi=-1}. \tag{49}$$

It is readily shown using (39) and (45*f*) that at the stagnation point $\xi = -1$, (37) reduces to

$$A_i \frac{\partial u_i}{\partial t} = \bar{\bar{T}} \frac{\partial^2 u_i}{\partial \hat{\eta}^2} + \bar{\bar{P}} \frac{\partial u_i}{\partial \hat{\eta}} + \chi_i, \tag{50}$$

where the A_i are defined by (45*h*–*j*); the χ_i are defined by (23) and are evaluated at $\xi = -1$. In addition,

$$\bar{\bar{T}} = \tilde{z}^2 \tilde{x}^2 Z^2, \quad \bar{\bar{P}} = \tilde{z}^2 Z^2 \left\{ \tilde{x} \frac{\partial \tilde{x}}{\partial \hat{\eta}} + \frac{Z'(\hat{\eta})}{Z(\hat{\eta})} \tilde{x}^2 + \frac{\tilde{x}^2}{\tilde{z}} \frac{\partial \tilde{z}}{\partial \hat{\eta}} \right\}, \tag{51}$$

with Z defined in (45*f*). The associated equations for the dependent variables $\tilde{x}$ and $\tilde{z}$ are

$$\frac{\partial}{\partial t}\{\log|\tilde{x}|\} = u_1 U'_\infty, \quad \frac{\partial}{\partial t}\{\log|\tilde{z}|\} = u_2 \tilde{W}_\infty, \tag{52}$$

with initial conditions

$$\tilde{x} = \tilde{z} = 1. \tag{53}$$

In (52), U'_∞ and $\tilde{W}_\infty$ are evaluated at $x = -1$.

4. Computational methods

The calculations were all started at $t = 0$ using the Eulerian formulation described in §2. A number of mesh sizes were used as a check on the accuracy, and the results presented here are based on a mesh with 201 and 101 points in the streamwise and normal directions, respectively, which was ultimately determined to provide good resolution; the accuracy was checked by running solutions on a 401 × 201 mesh. Typical values used for the time step were 0.001 and Crank–Nicolson approximations were made for the interior equations (25) and the stagnation-point equation (22) (written in terms of the variable $\hat{n}$). Central differences were used for all spatial derivatives, and the finite-difference approximations are therefore second-order accurate in space and time. The solution of (22) was first advanced a time step and then the solution of (25) was advanced using a factored alternating direction implicit (ADI) method similar to that described by Peridier *et al.* (1991). In transformation (24*b*), a stretching factor $k_n = 1$ was determined to be satisfactory, and preliminary calculations using the algebraic streamwise transformation suggested an intensifying region in the flow near $x = -1.8$; refined Eulerian calculations were then carried out using the tangent transformation (29) with $x_0 = -1.8$ and a stretching factor $k_x = 2/\pi$. The algebraic and tangent transformations with these values of x_0 and k_x will subsequently be referred to as mesh 1 and mesh 2, respectively.

During the initial development, the flow field is smooth and the algorithm passes through each time step in 2–3 global iterations; moreover, forward–backward differencing is not required. In general, calculations in the Eulerian formulation are easier to carry out and much more efficient than in the Lagrangian frame, provided that intense variations do not develop in the streamwise direction. Such variations do, however, start to occur as a boundary layer evolves toward separation, and eventually it proves impossible to obtain good resolution using the Eulerian formulation. It is worthwhile to note that in purely two-dimensional flows, the failure of the Eulerian algorithm is generally found to be fairly dramatic with the development of 'spiky' behaviour in the solution (see, for example, Doligalski & Walker 1984). However, the failure in the plane-of-symmetry flow considered here is somewhat more subtle, being characterized by the development of unrealistic wiggles of growing amplitude in the numerical solution, without an outright failure of the calculation. In fact, it proved possible to perform calculations in the Eulerian formulation with some meshes up to times beyond what was eventually determined to be the separation time t_s; at first glance, the calculated Eulerian results appeared to be plausible, but did not hold up under closer scrutiny. Thus, at least for the plane-of-symmetry flow considered here, incorrect numerical results are much easier to obtain than in known examples of two-dimensional separation.

The calculation scheme can be switched to the Lagrangian formulation at any time t_0, provided t_0 is not close to the separation time t_s. In the integrations, a separation singularity was ultimately detected at $t_s = 5.2$, to two significant figures. It is more efficient to remain in the Eulerian formulation for as long as possible, and calculations were carried out with switch times ranging from $t_0 = 3.5$ to 4.5; of course, the results must be essentially independent of the value of t_0 employed. At t_0 the initial values of the particle positions are given by (41). The same transformations were used in (24*a*) and (43*a*, *b*), and it follows that $\hat{x} = \hat{\xi}$ at $t = t_0$. Furthermore, since $y = \eta$ at $t = t_0$, using (12*a*), (24*b*) and (43*c*), it follows that

$$2t_0^{1/2} k_n \tan(\tfrac{1}{2}\pi\hat{n}) = k_\eta \tan(\tfrac{1}{2}\pi\hat{\eta}). \tag{54}$$

Consequently if the same mesh is used in $\hat{n}$ and $\hat{\eta}$ for both formulations, the stretching factor in the Lagrangian system is related to that adopted in the Eulerian system by

$$k_\eta = 2t_0^{1/2} k_n. \tag{55}$$

Therefore, the Eulerian solution for the u_i obtained from (22) and (25) was then used directly to initiate an integration of (50) and (44), respectively, forward in time within the Lagrangian system; in this manner, no interpolation is required to obtain the initial conditions. For the Lagrangian calculations, a second-order upwind–downwind scheme (Peridier *et al.* 1991) and a factored ADI method were used.

The Lagrangian formulation is most effective in regions of the boundary layer where the pressure gradient is adverse and sharply focused outflows start to develop. In regions of favourable pressure gradient or when relatively long periods of time elapse, the Lagrangian calculations tend to become less effective. This is because fluid particles which are initially close together eventually become far apart. In such circumstances, the gradients such as $\partial x/\partial\xi$ become large and the finite-difference equations associated with the approximations to (44) tend to become 'stiff' and lose the property of diagonal dominance; when this happens the progress of the iterations slows at each time step. This problem can be alleviated for a while by introducing forward–backward differencing for $\partial u_i/\partial\hat{\xi}$ and $\partial u_i/\partial\hat{\eta}$ as discussed by Peridier *et al.* (1991). However, unless the time step is progressively reduced to very small values, wiggles start to develop in the calculated results and soon the progress of the integration slows to an imperceptible crawl.

This problem can be avoided by periodically remeshing during the course of the Lagrangian integration. This process involves interrupting the Lagrangian integration and constructing the Eulerian field through the use of the continuity equation. This solution then serves as the new initial condition to initiate further Lagrangian calculations in the next cycle. It may be noted that remeshing can be done repeatedly, but the Eulerian solution must be fairly smooth since interpolation is involved in the process; thus remeshing must be avoided at times close to separation.

Remeshing is carried out as follows. The continuity equation (36) in computational coordinates is

$$\tilde{z}\left[\frac{\partial\hat{x}}{\partial\hat{\xi}}\frac{\partial\hat{y}}{\partial\hat{\eta}}-\frac{\partial\hat{x}}{\partial\hat{\eta}}\frac{\partial\hat{y}}{\partial\hat{\xi}}\right]=R=\frac{Z(\hat{y})}{Z(\hat{\eta})}\frac{h'_{\xi}(\hat{\xi})}{h'_{x}(\hat{x})}, \tag{56}$$

where the primes denote differentiation with respect to the argument. The characteristics are lines of constant $\hat{x}$ defined by

$$\frac{\mathrm{d}\hat{\eta}}{\tilde{z}(\partial\hat{x}/\partial\hat{\xi})}=\frac{\mathrm{d}\hat{\xi}}{\tilde{z}(-\mathrm{d}\hat{x}/\partial\hat{\eta})}=\frac{\mathrm{d}\hat{y}}{R}=\mathrm{d}\hat{s}, \tag{57}$$

where $\hat{s}$ is a parameter along the characteristic. These equations were integrated from the wall at $\hat{\eta}=0$ at any fixed value of t using a second-order predictor–corrector scheme to produce values of $\hat{y}(\hat{\xi},\hat{\eta},t)$ along lines of constant x. In these integrations the step in $\hat{s}$ was adjusted to produce values of $\hat{y}$ in equal increments. The values of u_i were obtained at these points through bilinear interpolation, hence providing the velocity and temperature field on a rectangular mesh in the $(\hat{x},\hat{y})$-plane; higher-order interpolation schemes were also used but were found to give essentially the same results, since the u_i fields are smooth and well-resolved with the spatial meshes used in the present integrations. The numerical details of the remeshing will be discussed subsequently.

5. Calculated results

Instantaneous streamlines in the upstream boundary layer for the plane-of-symmetry problem are shown in figure 2 at various times in the physical plane; for these results the switchover time from the Eulerian to Lagrangian calculations is $t_0=4$. These plots were obtained by first integrating (11 *a*) and (11 *c*) along lines of constant $\hat{x}$ to find ψ and ϕ, once the values of u_1 and u_2 were obtained on a rectangular $(\hat{x},\hat{y})$ grid; the normal velocity v is then calculated from (11 *b*). Immediately after the impulsive start, the instantaneous streamlines are deflected toward the endwall, and subsequently $\partial u_1/\partial y$ at $y=0$ becomes zero at $x=-1$ at $t=0.381$. Thereafter a saddle point of attachment appears on the wall (denoted by S1 in figure 2*a*) and subsequently moves upstream; since the limiting wall streamlines on the symmetry plane are toward this point while the spanwise flow is away from it, S1 is a three-dimensional point of attachment. Note that there is a corner region between the right boundary of the plot in figure 2(*a*) and the cylinder (as shown in figure 1 *a*); this region is passive (at least initially) and does not influence the solution in the upstream boundary layer. With the passage of time, the point of attachment moves progressively upstream. Eventually another saddle point S2 develops on the limiting streamline which terminates at the saddle point of attachment S1 as shown in figure 2(*b*). As shown in figure 2(*c*) a spiral focus (denoted by F1) opens up, and the saddle point S2 starts to move toward the wall as the point of attachment S1 continues to move upstream. This process continues as shown in figures 2(*d*), 2(*e*) and 2(*f*); it may be noted that as the spiral focus moves upstream, it appears to undergo a process of streamwise compression until at $t_s=5.2$ a separation singularity occurs. The evolution of the spiral focus on the symmetry plane is evidently the beginning of the formation of the necklace vortex observed in

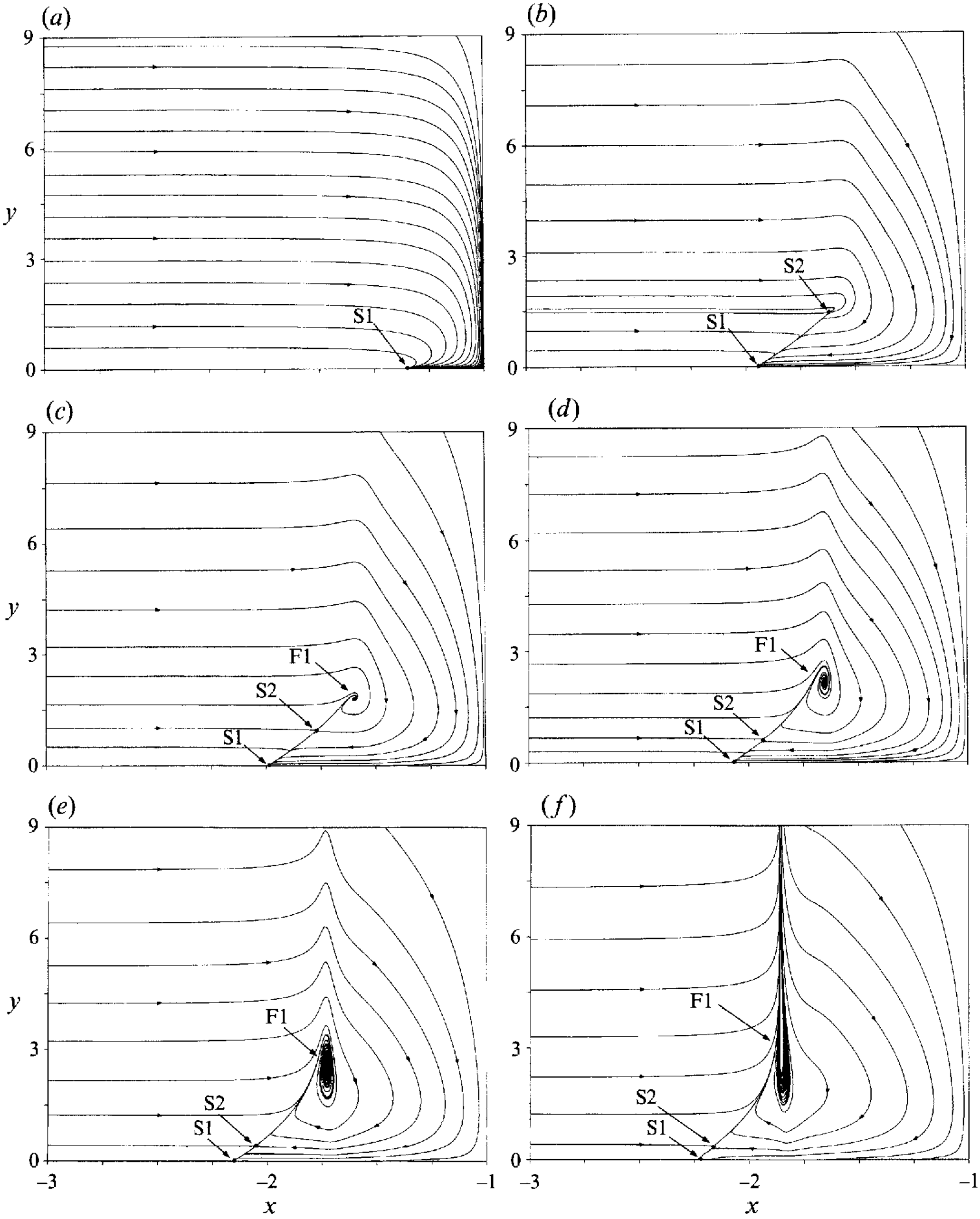

FIGURE 2. Evolution of the instantaneous streamlines on the upstream symmetry plane: (*a*) $t = 1.0$, (*b*) $t = 3.25$, (*c*) $t = 3.5$, (*d*) $t = 4.0$, (*e*) $t = 4.5$, (*f*) $t = t_s = 5.2$.

experiments (Smith *et al.* 1991). However, since the present study only treats the symmetry plane, it is not possible here to address the interesting question of how the developing vortex spreads out into the outboard endwall boundary layer. The instantaneous streamline patterns shown in figure 2 near the saddle point of attachment S1 are essentially similar to those found in Visbal's (1991) calculations of low and moderate Reynolds number flow, with the motion being characterized by flow toward the wall. As discussed by Visbal (1991), various authors have conjectured a

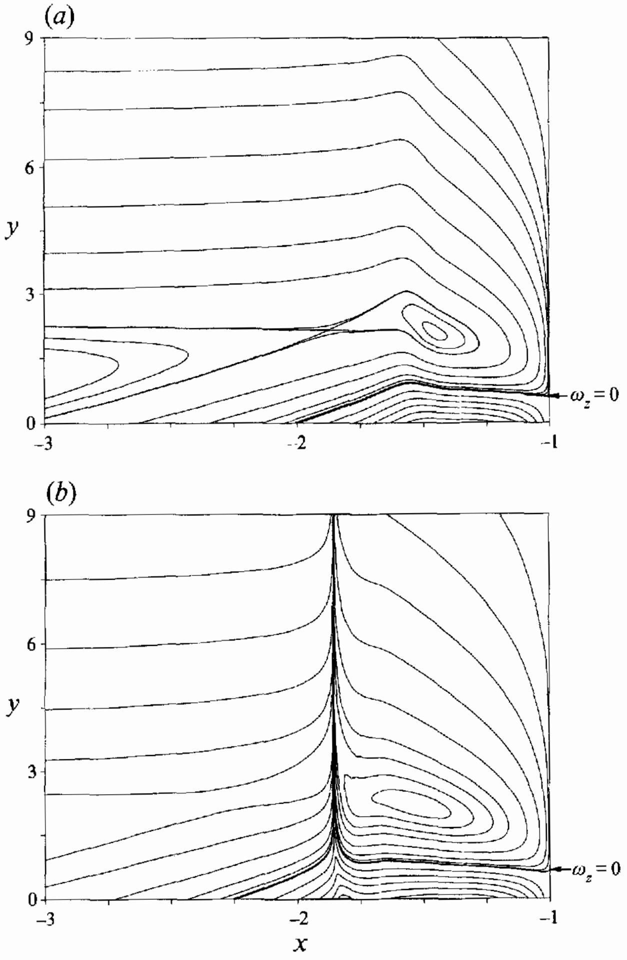

FIGURE 3. Equivorticity lines at (*a*) $t = 3.5$, (*b*) $t = t_s$.

'standard' streamline topology, in which S1 was a saddle point of separation (with flow away from the wall), in order to interpret certain flow visualization studies. The present results show that the 'new' topology described by Visbal (1991) is observed in the limit as $Re \rightarrow \infty$ and is therefore likely to be characteristic of a wide Reynolds number range. It may be noted that as the boundary layer evolves toward separation, the saddle point S2 does move very close to the wall and S1 (cf. figure 2*f*), thus almost giving the appearance of flow away from the wall. However, S2 does not reach S1 by t_s, and in a narrow region the flow is still toward S1 at the wall.

The sharp focusing of the boundary-layer flow into a band which is narrow in the streamwise direction is typical of separation phenomena in two-dimensional boundary layers (Van Dommelen & Shen 1980, 1982; Peridier *et al.* 1991); this behaviour will also be encountered in the present study of the boundary layer upstream of the two-dimensional ridge. The 'spiky' nature of the event in the plane-of-symmetry flow is not as prominent in the streamline patterns shown in figure 2(*f*) as in known two-dimensional realizations of boundary-layer separation. However, the sharply focused nature of the event can be seen in the temporal development of the vorticity field which is shown in figure 3. At $t = 3.5$ in figure 3(*a*), the contours of constant transverse vorticity, defined by $\omega_z = -\partial u/\partial y$ (to leading order in the boundary layer), are shown.

Throughout most of the field ω_z is negative, but there is a growing region of positive vorticity in the corner which is due to the reversal of the streamwise velocity there caused by the obstacle. There is a zero vorticity line $\omega_z = 0$ present in the field at $t = 3.5$, and theoretical considerations indicate (see Cowley *et al.* 1990) that if separation occurs, a singularity will develop somewhere along this line. Note that on the symmetry plane both of the other vorticity components are zero. In figure 3(*b*), the equivorticity lines are plotted just prior to separation, and it may be seen that the vorticity field and the zero vorticity line focus into a sharp spike, reminiscent of two-dimensional separation phenomena (Van Dommelen & Shen 1980, 1982; Peridier *et al.* 1991) and predicted by three-dimensional theories (Van Dommelen & Cowley 1990; Cowley *et al.* 1990).

The solution of the continuity equation (56) may be written in the form

$$\hat{y}(\hat{\xi}, \hat{\eta}, t) = \int_{wall}^{(\xi,\eta)} \frac{\mathrm{d}\hat{s}}{\tilde{z}R\{\hat{x}_{\hat{\xi}}^2 + \hat{x}_{\hat{\eta}}^2\}^{1/2}}, \tag{58}$$

where the integral is along a path of constant x passing through (ξ, η) and originating on the wall. It is evident that a singularity occurs at $t = t_s$ when either

$$\frac{\partial \hat{x}}{\partial \hat{\xi}} = \frac{\partial \hat{x}}{\partial \hat{\eta}} = 0 \quad \text{or} \quad \tilde{z} = 0 \quad \text{at} \quad \hat{\xi}_s, \hat{\eta}_s. \tag{59}$$

The first two conditions are the same as in two-dimensional flows, where they imply that a fluid particle (originating at (ξ_s, η_s)) has been compressed to zero streamwise thickness and has therefore grown infinitely long in a direction normal to the wall. In the plane of symmetry, severe streamwise compression is also implied by the first two conditions (59); however because a particle can also expand in the spanwise direction, the normal growth of the boundary layer is not as prominent as in two-dimensional flows. The third condition in (59) implies that the spanwise extent of the fluid particle is compressed to zero thickness, and once again the particle must grow infinitely large in the normal direction. However, this latter situation does not occur in the present problem, and only the first condition in (59) is satisfied with $\tilde{z}$ remaining positive everywhere for all times. Figure 4 shows the streamwise and cross-stream displacement thicknesses δ_1^* and δ_2^* defined by

$$\delta_1^* = \int_0^\infty (1-u_1)\,\mathrm{d}y, \quad \delta_2^* = \int_0^\infty (1-u_2)\,\mathrm{d}y. \tag{60}$$

It may be seen from figure 4 that both δ_1^* and δ_2^* develop sharp spikes at $t \to t_s$, with δ_2^* becoming large and negative. Using (11), it is easily shown that $\psi \sim U_\infty(y - \delta_1^*)$ and $\phi \sim \tilde{W}_\infty(y - \delta_2^*)$ as $y \to \infty$ and consequently

$$v \sim U_\infty \delta_1^{*\prime} + \tilde{W}_\infty(\delta_2^* - \delta_1^*) \quad \text{as} \quad y \to \infty, \tag{61}$$

where the fact that $U'_\infty + \tilde{W}_\infty = 0$ for the present problem has been used; here the primes denote differentiation with respect to x. In (61), the contribution associated with δ_2^* is negative for the times depicted in figure 4(*b*) with $t > 3$ (except in the immediate vicinity of the cylinder). Near the separation point $x = x_s$, the first term in (61) is positive for $x < x_s$ and negative for $x > x_s$, while the second term is negative. Thus the normal outflow from the boundary layer is diminished for $x < x_s$ by the second term in (61) while the inflow for $x > x_s$ is enhanced. This behaviour suggests why the eruptive response in the three-dimensional problem is relatively weaker than the corresponding event in the two-dimensional problem.

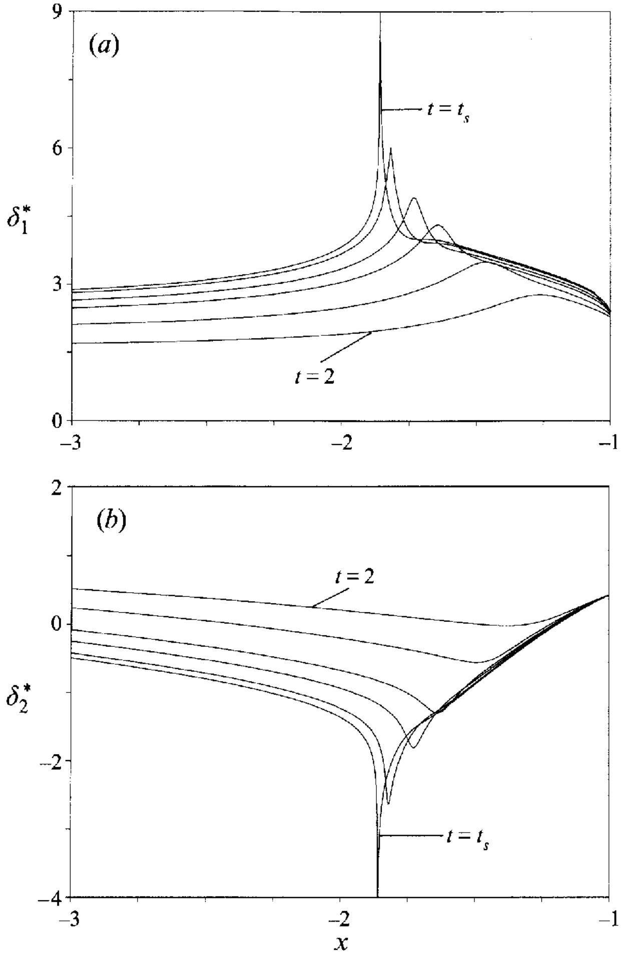

FIGURE 4. Temporal development of the (*a*) streamwise and (*b*) cross-stream displacement thicknesses; plotted curves are at $t = 2, 3, 4, 4.5, 5$, and $t_s = 5.2$.

The determination of the time of singularity, as well as the accurate evaluation of the solution properties as $t \to t_s$, was found to be considerably more challenging than the two-dimensional problem (to be discussed in §6). According to (59), a singularity is encountered when both $\partial\hat{x}/\partial\hat{\xi}$ and $\partial\hat{x}/\partial\hat{\eta}$ vanish simultaneously at a specific particle denoted by $(\hat{\xi}_s, \hat{\eta}_s)$. A number of methods of evaluation of the time of singularity were tried, but the most reliable method appears to be based on tracking the evolution of the two curves $\partial\hat{x}/\partial\hat{\xi} = 0$ and $\partial\hat{x}/\partial\hat{\eta} = 0$ and determining when and where these curves first touch. The curve $\partial\hat{x}/\partial\hat{\eta} = 0$ appears at an early stage in the calculation; however, $\partial\hat{x}/\partial\hat{\xi} = 0$ does not develop until the latter stages, and unless some care is taken, it appears as a narrow slit in the $(\hat{\xi}, \hat{\eta})$ computational plane. For example, when the algebraic transformation (28) was used in the Lagrangian calculations, the line $\partial\hat{x}/\partial\hat{\xi} = 0$ first appears in the $(\hat{\xi}, \hat{\eta})$-plane as a very narrow vertical slit of almost zero thickness, which does not change appreciably as $t \to t_s$; this means it is very difficult to resolve accurately the curve $\partial\hat{x}/\partial\hat{\xi} = 0$ (particularly near its vertical extremities), and this makes the time when it touches the curve $\partial\hat{x}/\partial\hat{\eta} = 0$ uncertain.

In order to rectify this difficulty, it is necessary to find a means to concentrate mesh points in the $\hat{\xi}$-direction in the vicinity of the fluid particle which ultimately becomes

	Algebraic	Tangent			
	Mesh 1	Mesh 2	Mesh 3	Mesh 4	Mesh 5
Points in $\hat{\xi}$	201	201	201	201	401
Points in $\hat{\eta}$	101	101	101	101	201
Time step	0.001	0.001	0.001	0.001	0.0005
k_ξ	—	$2/\pi$	$1/\pi$	$1/2\pi$	$1/2\pi$
ξ_o	—	-1.8	-1.83	-1.8265	-1.8265

TABLE 1. Details of the meshes used for Lagrangian calculations for the upstream plane-of-symmetry flow

compressed to zero streamwise thickness at separation. To this end, consider the following transformation:

$$\xi = \hat{h}_\xi(\hat{\xi}) = \xi_o + k_\xi \tan\left\{\frac{\pi}{2}\left(\frac{\hat{\xi}}{\hat{\xi}_o} - 1\right)\right\}, \tag{62}$$

where for $\xi = -1$ to correspond to $\hat{\xi} = 1$,

$$\frac{1}{\hat{\xi}_o} = 1 + \frac{2}{\pi}\arctan\left(\frac{-1-\xi_o}{k_\xi}\right), \tag{63}$$

which is analogous to (29) and (30). Here k_ξ is a parameter controlling the mesh distribution, and the range $(-\infty, -1]$ in ξ is transformed by (62) to $(0, 1]$ in $\hat{\xi}$, with a concentrated mesh near ξ_o in physical space. Since the ξ-location of the particle which is ultimately compressed is not known *a priori*, it proved necessary to adopt the iterative strategy outlined below. Suppose the calculation was switched from the Eulerian to the Lagrangian mode at t_0; the Lagrangian calculation was then continued using a remeshing procedure every 0.5 units in time and the equivalent of the algebraic transformation (28) in ξ. This mesh is designated as mesh 1 and a calculation was carried out on it until a singularity was predicted. From this calculation, an estimate of $\xi_s = -1.8$ was obtained. The Eulerian calculations were initiated once again from impulsive start with $x_0 = \xi_o = -1.8$ and $k_x = 2/\pi$ (for reference, see (29) and (30)). The Eulerian solution at t_0 was then used as initial conditions to start the Lagrangian calculations with $\xi_o = \xi_s$ and $k_\xi = 2/\pi$. This calculation with the tangent transformation and aforementioned values of ξ_o and k_ξ is subsequently referred to as mesh 2. The solution with mesh 2 produced a refinement for ξ_s which was subsequently used to initiate a third computation. In this manner, a total of five meshes were used; the stretching factor k_η is evaluated from (55). Note that meshes 3–5 utilize the remeshed solution from mesh 2 as an initial condition at $t = 4$ (rather than returning all the way back to impulsive start in Eulerian coordinates). The mesh sizes listed in table 1 were found to produce accurate results; furthermore, the local packing algorithm (62) was judged to be much more effective for the success of the scheme than simply increasing the number of spatial points in the streamwise direction.

The results of the calculation are shown in table 2. It may be seen that the results from mesh 1 are in reasonable agreement with each other for different values of t_0; however, the results eventually converge to somewhat different values from mesh 1 as the mesh is systematically refined. The final estimated values are $t_s = 5.2$, $x_s = -1.86$, $u_s = -0.18$ and $\tilde{w}_s = 0.52$. Consequently the fluid particle which is compressed at separation is moving upstream and expanding away from the symmetry plane at t_s,

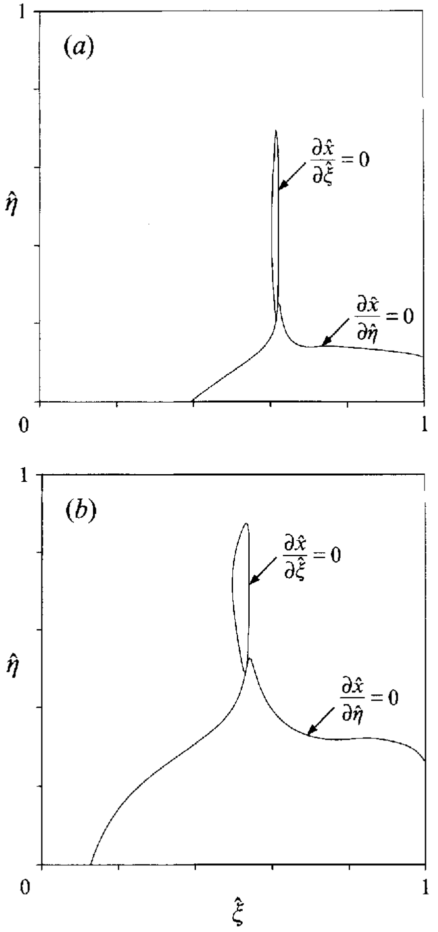

FIGURE 5. Plotted curves $\partial \hat{x}/\partial \hat{\xi} = 0$ and $\partial \hat{x}/\partial \hat{\eta} = 0$ just prior to predicted separation time for $t_o = 4$: (*a*) mesh 2, (*b*) mesh 4.

t_o	Mesh 1	Mesh 2	Mesh 3	Mesh 4	Mesh 5
3.5	$t_s = 5.432$	5.286	5.251	5.219	5.183
	$x_s = -1.900$	−1.876	−1.869	−1.864	−1.857
	$u_s = -0.185$	−0.192	−0.175	−0.185	−0.185
	$\tilde{w}_s = 0.506$	0.535	0.510	0.526	0.529
4.0	$t_s = 5.435$	5.290	5.218	5.203	5.191
	$x_s = -1.900$	−1.876	−1.863	−1.861	−1.858
	$u_s = -0.185$	−0.189	−0.189	−0.182	−0.185
	$\tilde{w}_s = 0.506$	0.530	0.531	0.524	0.529
4.5	$t_s = 5.450$	5.303	5.241	5.224	5.217
	$x_s = -1.902$	−1.878	−1.867	−1.864	−1.863
	$u_s = -0.185$	−0.184	−0.191	−0.183	−0.187
	$\tilde{w}_s = 0.505$	0.523	0.531	0.522	0.529

TABLE 2. Calculated results for the plane of symmetry

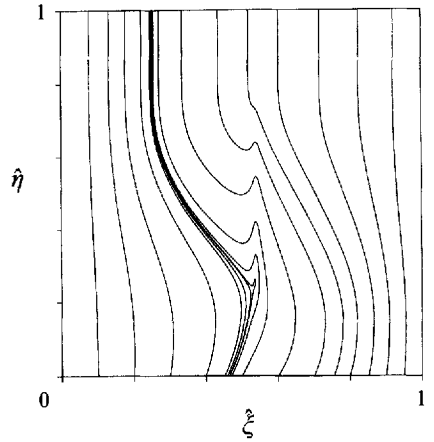

FIGURE 6. Contours of constant $\hat{x}$ in the computational plane.

as suggested by the temporal development of the displacement functions shown in figure 4.

The main advantage of the present iterative scheme in determining t_s and the properties at separation is illustrated in figure 5. In figure 5(*a*), the results of a calculation with $t_0 = 4$ for mesh 2 is shown; the vertical slit represents the curve $\partial\hat{x}/\partial\hat{\xi} = 0$, and at t_s the curve just touches the curve $\partial\hat{x}/\partial\hat{\eta} = 0$ (in the lower half of the figure). The situation in figure 5(*a*) constitutes a considerable improvement over that which had been obtained using the algebraic transformation mesh 1; the algebraic mesh emphasizes the region near $x = -1$ where exponential growth in the boundary layer eventually occurs. Mesh 1 was used in a preliminary calculation to estimate $\hat{\xi}_s$; the results are not shown here, but it was found that the curve $\partial\hat{x}/\partial\hat{\xi} = 0$ appeared as a slit of almost zero thickness, which is difficult to resolve accurately. This behaviour makes the accurate determination of the instant when the two curves touch problematic. Further improvement is evident in the refined mesh 4 calculation shown in figure 5(*b*). As a result of mesh packing near the particle which is eventually compressed, the curve $\partial\hat{x}/\partial\hat{\xi} = 0$ is now considerably expanded and better defined. Thus at separation an accurate evaluation of when the two curves touch at $t = t_s$ is possible. Curves of constant $\hat{x}$ are shown in figure 6 for calculations based on mesh 5; the singularity occurs inside a small thumb at $\hat{\xi}_s = 0.535$ and $\hat{\eta}_s = 0.245$ (where $\hat{\xi}_s$, $\hat{\eta}_s$ denote the location of the particle that undergoes separation at the last remesh, which in this case is at $t = 5$). Note that unlike known two-dimensional realizations of separation (Van Dommelen & Shen, 1980, 1982; Peridier *et al.* 1991), the thumb in the x-characteristic surrounding the singular point is very narrow (even though a transformation to expand the region near $\hat{\xi}_s$ has been employed here). In addition, the x-characteristics above the singular point also show a narrowed distention well into the upper parts of the boundary layer.

Calculated results for the temporal development of wall shear stress in the streamwise ($\tau_{wx} = \partial u/\partial y$ at $y = 0$) and cross-stream ($\tilde{\tau}_{wz} = \partial\tilde{w}/\partial y$ at $y = 0$) directions are shown in figure 7. It may be seen that a local decrease occurs in the streamwise wall shear stress and a local increase occurs in the spanwise gradient of the cross-stream wall shear stress near separation; however, the behaviour is smooth and as in two-dimensional flows (Van Dommelen & Shen 1982; Elliott *et al.* 1983), the wall shear stress is regular as $t \rightarrow t_s$. A similar behaviour occurs in the wall heat transfer rate $\partial\theta/\partial y$

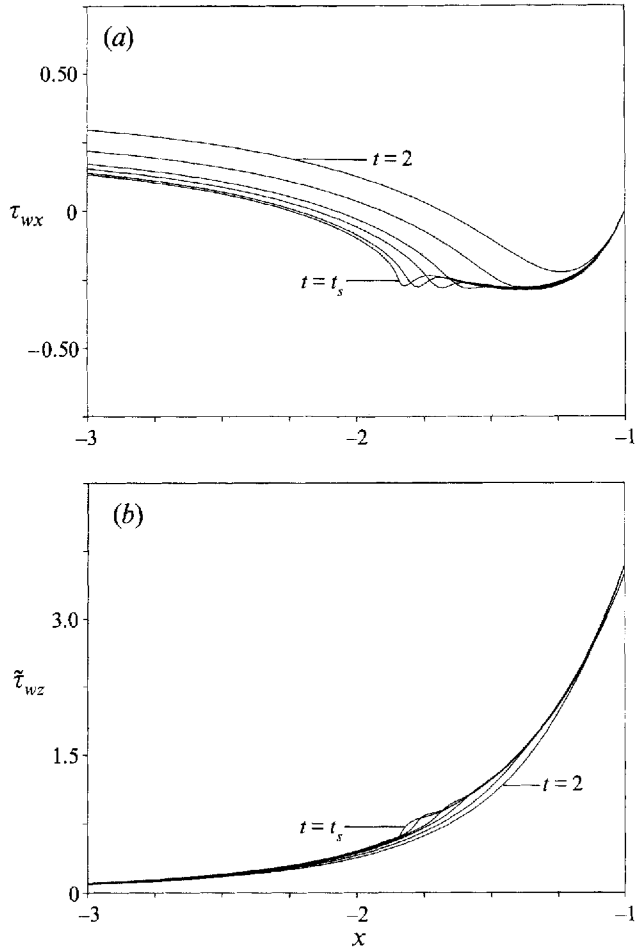

FIGURE 7. Wall shear stress in the plane of symmetry at $t = 2$, 3, 4, 4.5, 5 and $t_s = 5.2$: (*a*) streamwise shear stress, (*b*) spanwise gradient of the cross-stream shear stress.

at $y = 0$ shown in figure 8(*a*), which is also regular but begins to develop a strong local minimum at the streamwise location of separation. The reason may be seen in figure 8(*b*) where the constant-temperature contours at t_s are shown. The dramatic upwelling at separation pulls the contours into a narrow streamwise band, and this results in a relatively low heat flux at $x = x_s$. Note that to the right of x_s the heat transfer rates are relatively high especially near the cylinder. Here fluid from the mainstream, having a temperature different from that on the wall, sweeps into the corner giving rise to enhanced heat transfer through both convection and conduction effects.

6. The cylindrical ridge

As indicated schematically in figure 1(*b*), three boundary layers develop independently near the circular ridge after the impulsive start. Discontinuities in the bottom topography occur at $x = \pm 1$, and the mainstream velocity distribution for both the upstream and downstream boundary layers (regions 1 and 3 in figure 1*b*) is given by (10*a*). Again the downstream boundary layer experiences a continuously favourable pressure gradient and is of much less interest than the upstream boundary layer where

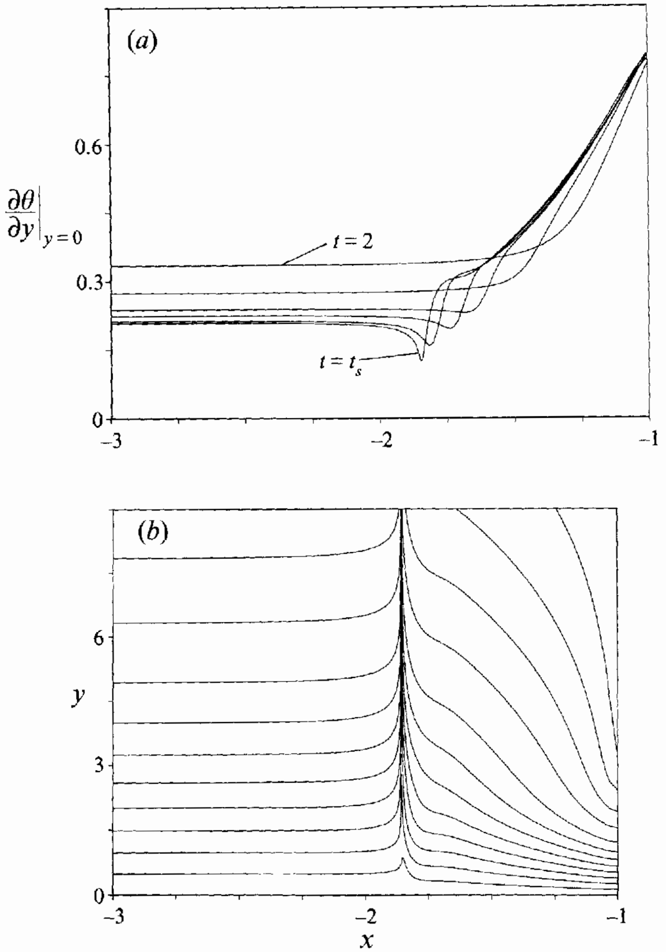

FIGURE 8. Heat transfer characteristics in the plane of symmetry. (*a*) Temporal development of surface heat flux at $t = 2$, 3, 4, 4.5, 5 and $t_s = 5.2$. (*b*) Contours of constant temperature at t_s.

	Streamwise transformation	
t_0	Algebraic	Tangent
1.7	$t_s = 2.712$	2.714
	$x_s = -1.602$	−1.603
	$u_s = -0.355$	−0.359
2.0	$t_s = 2.714$	2.717
	$x_s = -1.603$	−1.604
	$u_s = -0.356$	−0.357
2.3	$t_s = 2.722$	2.724
	$x_s = -1.605$	−1.606
	$u_s = -0.353$	−0.358

TABLE 3. Calculated results for the circular ridge

$\mathrm{d}p_\infty/\mathrm{d}x$ is purely adverse. On the half-cylinder itself, the mainstream velocity distribution is $U_\infty = -2\sin\theta$, and as described by Van Dommelen & Shen (1980, 1982), a separation singularity is encountered at $\theta \approx 69°$ at $t_s \approx 1.5$. Here the objective is to determine the evolution of the upstream boundary layer and compare the results with both the development on the cylinder itself and the corresponding plane-of-symmetry results.

The equations governing the upstream boundary layer may be obtained from those given in §§2 and 3 by taking $\tilde{w}$, $\tilde{W}_\infty \equiv 0$ (for example, in (8) and (37*b*)). Both the tangent transformation (29) and the algebraic transformation (28) were used in the two-dimensional problem; however, because strong exponential boundary-layer growth ultimately occurs at the stagnation point at $x = -1$, the algebraic transformation was found to be preferable since it emphasizes the zone near $x = -1$. Again a number of mesh sizes were tried as a check on the accuracy and the results presented are based on a mesh with 201 and 101 points in the streamwise and normal directions respectively; a time step of 0.001 units in both the Eulerian and Lagrangian integrations was found to be small enough to ensure grid-independent results. A separation singularity was encountered at $t_s \approx 2.71$ and the relevant calculated values of the solution are given in table 3, where again t_0 denotes the time at which the calculation was switched from the Eulerian to the Lagrangian system. Lagrangian calculations for the two-dimensional problem are much easier than the corresponding plane-of-symmetry problem and re-meshing in the Lagrangian formulation was not necessary. In the tangent transformation, $k_x = k_\xi = 2/\pi$ was used, and ξ_0 was based on the estimate of the singularity location obtained using the algebraic transformation; a value of $k_n = 1.0$ was used in the normal transformation (24*b*). It follows from table 3 that the estimates of $t_s = 2.71$, $x_s = -1.60$ and $u_s = -0.36$ are correct to the digits quoted. The case where the switch to the Lagrangian frame was performed at $t_0 = 2.3$ is believed to be somewhat too late, with the Eulerian solution possibly containing significant error due to the sharp spatial gradients which develop by that stage. Although both the algebraic and tangent transformations give similar results for the separation properties, the algebraic transformation yields much smoother answers at the stagnation point where the boundary-layer thickness is growing very rapidly near the end of the calculation. The work of Van Dommelen & Shen (1980, 1982) shows that the boundary layer on the half-cylinder will become eruptive at $t \approx 1.5$, leading to an ejection of vorticity into the mainstream; however, the eruption is predicted on the rear portion of the cylinder, and the subsequent alterations produced in the external flow should not be substantial in the inviscid flow region above the upstream boundary layer. The present calculations show that the upstream boundary layer will become eruptive at $t = 2.71$, which is almost twice as long as the time required for the eruption on the cylinder itself. Consequently, it might be expected that in a high Reynolds number flow, almost periodic boundary-layer eruptions will be observed in this geometry with roughly twice as many ejections of vorticity occurring on the cylinder as in the upstream boundary layer.

Calculated streamline patterns are shown in figure 9. A reversed-flow region develops in the corner starting at $t = 0.332$ and grows substantially with the passage of time. The situation at $t = 1.5$ is shown in figure 9(*a*) where one of the stagnation points associated with the region of reversed flow has moved far from the bottom wall along the line $x = -1$; the semi-similar solution on $x = -1$ corresponds to that described by Proudman & Johnson (1962) (see also Van Dommelen & Shen 1985) and here the boundary-layer thickness eventually grows exponentially with time. The other stagnation point on the wall moves progressively upstream as the reversed-flow region propagates away from the obstacle. At $t = 2.4$, a kinking of the streamlines may be

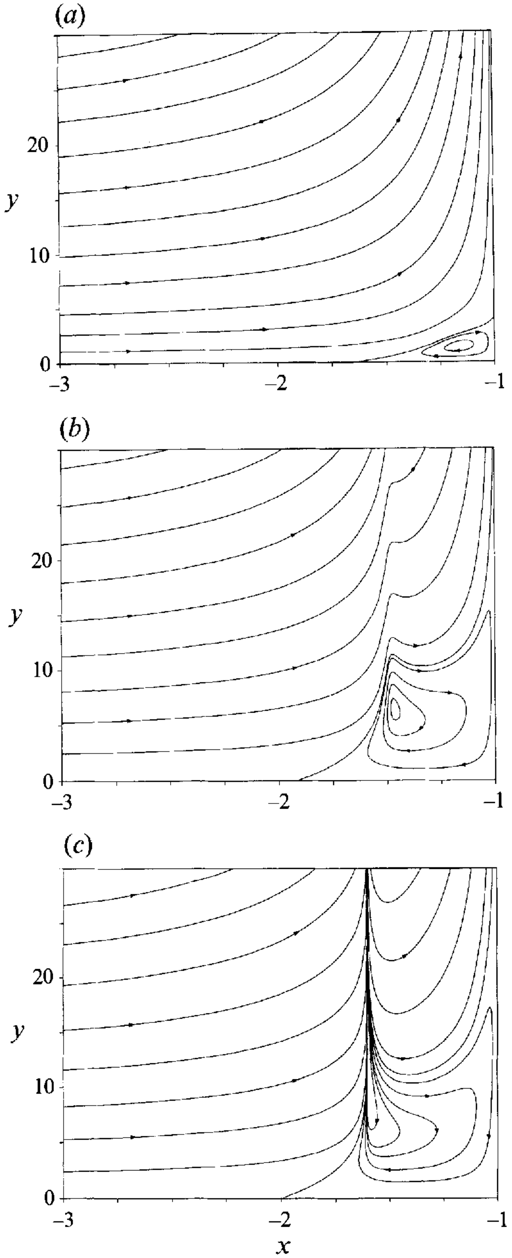

FIGURE 9. Instantaneous streamlines in the boundary layer upstream of a circular ridge: (*a*) $t = 1.5$, (*b*) $t = 2.4$, (*c*) $t = t_s = 2.71$.

seen in figure 9(*b*) on the upstream side of the reversed-flow region; by $t = 2.71$ a separation singularity occurs with the boundary-layer flow focusing into a narrow eruptive band as shown in figure 9(*c*). Since $u_s < 0$, this situation is a case of 'upstream-slipping' separation as is evident from the temporal development of the displacement thickness δ_1^* shown in figure 10. Computed values of the wall shear stress show a smooth and regular behaviour at $t \rightarrow t_s$, as predicted by Elliott *et al.* (1983) and Van Dommelen & Shen (1980, 1982). A similar smooth behaviour occurs for the wall heat

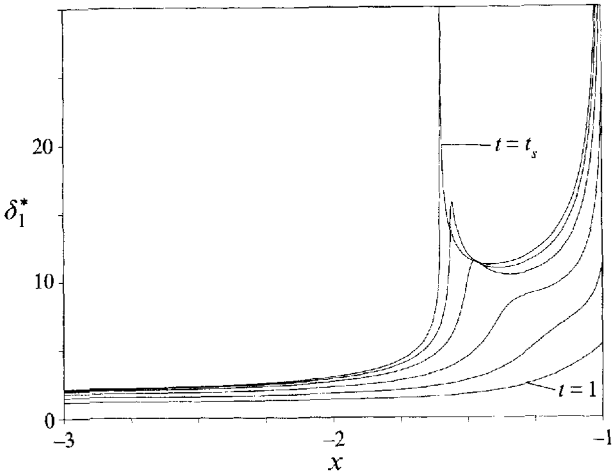

FIGURE 10. Temporal development of the displacement thickness for $t = 1, 1.5, 2, 2.4, 2.6$ and $t_s = 2.71$.

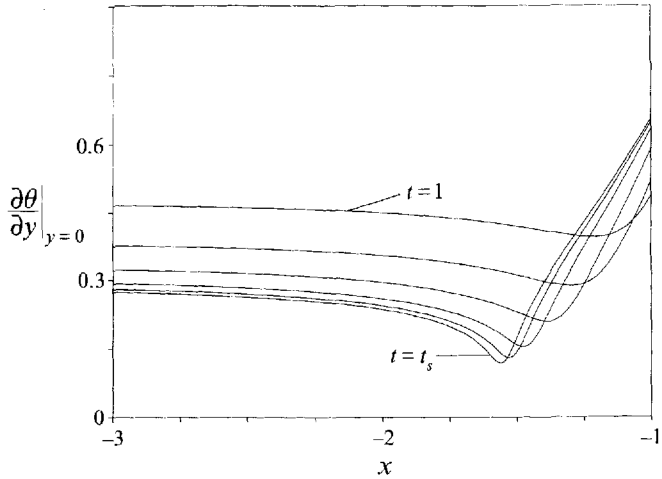

FIGURE 11. Temporal development of the surface heat flux for $t = 1, 1.5, 2, 2.4, 2.6$ and $t_s = 2.71$.

flux whose temporal development is shown in figure 11. It may be noted that again relatively high values of heat flux are achieved near the inviscid stagnation point, while the separation leads to a region of progressively decreasing heat flux that continuously moves upstream.

7. Conclusions

In the present study, the nature of the unsteady boundary-layer flow upstream of an upright cylinder mounted on a flat plate and a two-dimensional circular ridge has been considered. It has been shown that a separation singularity develops in the boundary-layer solution at a finite time after the impulsive start in both cases. This indicates that a boundary-layer eruption and subsequent unsteady viscous–inviscid interaction will occur; thus the flow upstream of such obstacles is inherently unsteady for large Reynolds numbers. In the three-dimensional problem, separation was found to occur on the upstream symmetry plane of the obstacle in a manner consistent with recent experimental observations and which is suggestive of the process by which necklace vortices seem to originate near the symmetry plane (Smith *et al.* 1991; Doligalski *et al.* 1994). To understand the complete development, it will eventually be necessary to evaluate the outboard development of this process in the endwall boundary layer. It may be noted that three-dimensional unsteady boundary layers can develop complex separation patterns (see, for example, Affes, Xiao & Conlisk 1994) and especially complicated topologies are expected in the present three-dimensional problem (Smith *et al.* 1991).

It is worthwhile to remark that the corresponding separation in two dimensions for the circular ridge is a much more dramatic and stronger event than for the symmetry plane, even though the streamwise mainstream velocity is the same for both flows. In the two-dimensional problem, the Eulerian calculations fail to converge before separation, and this failure gives a clear signal that a switch to the Lagrangian formulation is needed. On the other hand, the failure of the Eulerian scheme in the plane of symmetry is much more subtle with small wiggles developing in the numerical solution that cannot be removed by further grid refinement. Indeed, the Eulerian calculations could be carried on well beyond t_s without obvious difficulties, producing apparently plausible answers that at first glance even appear to be consistent with experiment; for example, a computed Eulerian solution at $t = 6$ suggested that the spiral focus (cf. figure 2*f*) continues to move further upstream with a second spiral focus developing behind it. Of course, the Lagrangian calculations clearly show that a singularity occurs at $t_s = 5.2$, thereby terminating the validity of the present boundary-layer formulation and pointing to a need for an interactive strategy with the mainstream flow. A main point here is that it is very much easier to obtain incorrect results using the Eulerian formulation with a fixed grid in the three-dimensional flow than in two dimensions; at the least, some type of adaptive grid (see, for example, Adams *et al.* 1995) would be necessary to improve the performance of the Eulerian method.

Although the present calculations have been carried out for two specific obstacles, experiments and theoretical considerations suggest that similar behaviour will occur over a range of shapes that have an $O(1)$ discontinuity in bottom topography where the obstacle is joined to the wall (Doligalski *et al.* 1994). The inviscid solution for lenticular two-dimensional obstacles is given by Milne-Thomson (1962, pp. 171–175) and three-dimensional obstacles such as airfoil shapes and rectangular blocks will give rise to an adverse pressure gradient on the symmetry plane similar to those considered here; hence the boundary-layer structure for a variety of obstacles will be similar to that shown in figure 1, and the boundary-layer response should be analogous. The calculated results for heat transfer indicate that the region upstream of obstacles will be an area of relatively high thermal stress. This is because the separation process that is expected to occur intermittently in such regions gives rise to alternate zones of relatively high and low heat transfer; the heat transfer is always largest adjacent to the stagnation point, but is dramatically reduced in a narrow streamwise band near separation. An additional contributing factor to thermal stress is that the zone of low heat transfer is in continual motion upstream as the separation process develops during each cycle.

The authors are grateful for support of this work under AFOSR Grant Numbers 91-0218 and F49620-93-1-0217.

Appendix

The transformation to the Lagrangian frame and the inverse transformation may be described by relations of the form

$$\begin{bmatrix} \mathrm{d}x \\ \mathrm{d}y \\ \mathrm{d}z \end{bmatrix} = \boldsymbol{A} \begin{bmatrix} \mathrm{d}\xi \\ \mathrm{d}\eta \\ \mathrm{d}\zeta \end{bmatrix}, \quad \begin{bmatrix} \mathrm{d}\xi \\ \mathrm{d}\eta \\ \mathrm{d}\zeta \end{bmatrix} = \boldsymbol{B} \begin{bmatrix} \mathrm{d}x \\ \mathrm{d}y \\ \mathrm{d}z \end{bmatrix}, \tag{A 1a,b}$$

where $\boldsymbol{A}$ and $\boldsymbol{B}$ are defined by

$$\boldsymbol{A} = \begin{bmatrix} x_\xi & x_\eta & x_\zeta \\ y_\xi & y_\eta & y_\zeta \\ z_\xi & z_\eta & z_\zeta \end{bmatrix}, \quad \boldsymbol{B} = \begin{bmatrix} \xi_x & \xi_y & \xi_z \\ \eta_x & \eta_y & \eta_z \\ \zeta_x & \zeta_y & \zeta_z \end{bmatrix}. \tag{A 2a,b}$$

Here the subscripts denote partial derivatives, and it is evident from (A 1) that $\boldsymbol{B} = \boldsymbol{A}^{-1}$. Using (33) which pertain to a symmetry-plane flow, an expression for $\boldsymbol{A}^{-1}$ may be obtained by inversion of (A 2*a*), namely

$$\boldsymbol{B} = \frac{1}{J} \begin{bmatrix} y_\eta z_\zeta & -x_\eta z_\zeta & x_\eta y_\zeta - y_\eta x_\zeta \\ -y_\xi \zeta_\zeta & x_\xi z_\zeta & -x_\xi y_\zeta + y_\xi x_\zeta \\ 0 & 0 & x_\xi y_\eta - x_\eta y_\xi \end{bmatrix}. \tag{A 3}$$

Here $J = |\boldsymbol{A}|$ is the Jacobian of the transformation given by

$$J = \left| \frac{\partial(x,y,z)}{\partial(\xi,\eta,\zeta)} \right| = z_\zeta(x_\xi y_\eta - x_\eta y_\xi). \tag{A 4}$$

Using (A 3), it is easily shown that the gradients transform according to

$$\frac{\partial}{\partial x} = \frac{1}{J}\frac{\partial z}{\partial \zeta}\left(\frac{\partial y}{\partial \eta}\frac{\partial}{\partial \xi} - \frac{\partial y}{\partial \xi}\frac{\partial}{\partial \eta}\right), \quad \frac{\partial}{\partial y} = \frac{1}{J}\frac{\partial z}{\partial \zeta}\left(-\frac{\partial x}{\partial \eta}\frac{\partial}{\partial \xi} + \frac{\partial x}{\partial \xi}\frac{\partial}{\partial \eta}\right), \tag{A 5a,b}$$

$$\frac{\partial}{\partial z} = \frac{1}{J}\left(\frac{\partial x}{\partial \xi}\frac{\partial y}{\partial \eta} - \frac{\partial x}{\partial \eta}\frac{\partial y}{\partial \xi}\right)\frac{\partial}{\partial \zeta}. \tag{A 5c}$$

Upon substitution of these relations and the Lagrangian definitions of velocity

$$u = \frac{\partial x}{\partial t'}, \quad v = \frac{\partial y}{\partial t'}, \quad w = \frac{\partial z}{\partial t'}, \tag{A 6}$$

into the continuity equation, it is easily shown that on the symmetry plane $\partial J/\partial t' = 0$. Since the particle positions are defined at some initial instant by

$$x = \xi, \quad y = \eta, \quad z = \zeta, \tag{A 7}$$

it follows from equation (A 4) that $J \equiv 1$ for all t'. Consequently, from (32) and (A 4), the continuity equation in the plane of symmetry is given by (36).

The Lagrangian time derivative is related to the substantive derivative in the Eulerian formulation by

$$\frac{\partial}{\partial t'} = \frac{\partial}{\partial t} + u\frac{\partial}{\partial x} + v\frac{\partial}{\partial y} + w\frac{\partial}{\partial z}, \tag{A 8}$$

and using (A 5*b*) (with $J = 1$), as well as (34) and (35), it is easily shown that the momentum and energy equations are given by (37).

REFERENCES

ACARLAR, M. S. & SMITH, C. R. 1987 A study of hairpin vortices in a laminar boundary layer. Part 1. Hairpin vortices generated by a hemisphere protuberance. *J. Fluid Mech.* **175**, 1–41.

ADAMS, E. C., CONLISK, A. T. & SMITH, F. T. 1995 Adaptive grid scheme for vortex-induced boundary layers. *AIAA J.* **33**, 864–870.

AFFES, H., XIAO, Z. & CONLISK, A. T. 1994 The boundary-layer flow due to a vortex approaching a cylinder. *J. Fluid Mech.* **275**, 33–57.

COWLEY, S. J., VAN DOMMELEN, L. L. & LAM, S. T. 1990 On the use of Lagrangian variables in descriptions of unsteady boundary-layer separation. *Phil. Trans. R. Soc. Lond.* A **333**, 343–378.

DOLIGALSKI, T. L. & WALKER, J. D. A. 1984 The boundary layer induced by a convected two-dimensional vortex. *J. Fluid Mech.* **139**, 1–28.

DOLIGALSKI, T. L., SMITH, C. R. & WALKER, J. D. A. 1994 Vortex interactions with walls. *Ann. Rev. Fluid Mech.* **26**, 573–616.

ELLIOTT, J. W., COWLEY, S. J. & SMITH, F. T. 1983 Breakdown of boundary layers: (i) on moving surfaces; (ii) in self-similar unsteady flow; (iii) in fully unsteady flow. *Geophys. Astrophys. Fluid Dyn.* **25**, 77–138.

ERSOY, S. & WALKER, J. D. A. 1987 The boundary layer due to a three-dimensional vortex loop. *J. Fluid Mech.* **185**, 569–598.

HUNG, C. M., SUNG, C. H. & CHEN, C. L. 1991 Computation of saddle point of attachment. *AIAA Paper* 91–1713.

MILNE-THOMSON, L. M. 1960 *Theoretical Hydrodynamics*, 4th edn. Macmillan.

PERIDIER, V. J., SMITH, F. T. & WALKER, J. D. A. 1991 Vortex-induced boundary-layer separation. Part 1: The limit problem $Re \to \infty$. *J. Fluid Mech.* **232**, 99–131.

PROUDMAN, I. & JOHNSON, K. 1962 Boundary-layer growth near a rear stagnation point. *J. Fluid Mech.* **12**, 161–168.

SEARS, W. P. & TELIONIS, D. P. 1975 Boundary-layer separation in unsteady flow. *SIAM J. Appl. Maths* **28**, 215–235.

SMITH, C. R., FITZGERALD, J. P. & GRECO, J. J. 1991 Cylinder end-wall vortex dynamics. *Phys. Fluids* A **3**, 2031.

VAN DOMMELEN, L. L. & COWLEY, S. J. 1990 On the Lagrangian description of unsteady boundary-layer separation. Part 1. General theory. *J. Fluid Mech.* **210**, 593–626.

VAN DOMMELEN, L. L. & SHEN, S. F. 1980 The spontaneous generation of the singularity in a separating boundary layer. *J. Comput. Phys.* **38**, 125–140.

VAN DOMMELEN, L. L. & SHEN, S. F. 1982 The genesis of separation. In *Proc. Symp. on Numerical and Physical Aspects of Aerodynamic Flow* (ed. T. Cebeci), *Long Beach, California*, pp. 283–311. Springer.

VAN DOMMELEN, L. L. & SHEN, S. F. 1985 The flow at a near stagnation point is eventually determined by exponentially small values of velocity. *J. Fluid Mech.* **157**, 1–16.

VISBAL, M. R. 1991 Structure of laminar juncture flows. *AIAA J.* **29**, 1273–1282.